Mixed QCD-electroweak contributions to Higgs-plus-dijet production at the CERN LHC

A. Bredenstein,[1] K. Hagiwara,[1,2] and B. Jäger[1]

[1]*KEK Theory Division, Tsukuba 305-0801, Japan*

[2]*Graduate University of Advanced Studies (Sokendai), Tsukuba 305-0801, Japan*

(Received 29 January 2008; published 8 April 2008)

We present a calculation of interference effects in Hjj production via gluon fusion and via vector boson fusion, respectively, beyond tree level. We reproduce results recently discussed in the literature, but go beyond this calculation by including a class of diagrams not considered previously. Special care is taken in developing a numerically stable and flexible parton-level Monte Carlo program which allows us to study cross sections and kinematic distributions within experimentally relevant selection cuts. Loop-induced interference contributions are found to exhibit kinematical distributions different in shape from vector boson fusion. Because of the small interference cross section and cancellation among different quark flavor contributions, their impact on the signal process is found to be negligible in all regions of phase space, however.

DOI: 10.1103/PhysRevD.77.073004 PACS numbers: 14.80.Bn, 12.38.Bx

I. INTRODUCTION

Higgs production via weak boson fusion (WBF), i.e., the reaction $pp \to Hjj$, mediated by t-channel weak boson exchange, constitutes a particularly promising production mechanism for the Higgs boson. Because of the distinctive signature of two hard jets accompanying the decay products of the Higgs boson, this channel is discussed as a possible discovery mode for a scalar, CP-even boson as predicted by the standard model (SM) [1,2], and as powerful tool for a later determination of its couplings [3]. Furthermore, WBF could be employed in studying deviations from the SM expectations and help to spot signatures of physics beyond the standard model. This can only be achieved, however, if accurate measurements are matched by precision calculations of SM signal and background processes and predictions for possible new physics scenarios.

Next-to-leading order (NLO) QCD corrections to the SM $pp \to Hjj$ WBF signal are available for cross sections [4] and distributions [5]. At the same level of accuracy, some of the most important background processes such as Vjj [6] and $VVjj$ [7] production in WBF, $t\bar{t}$ [8] and $t\bar{t}j$ [9] production are known. Beyond the standard model, Monte Carlo studies have been performed for WBF Hjj production in the presence of anomalous gauge boson couplings [10] and in the context of supersymmetric models [11]. Recently, NLO electroweak (EW) corrections for cross sections and distributions have been presented [12]. Finite parts of the next-to-next-to-leading order (NNLO) QCD corrections have been calculated in [13] and found to be negligible.

An irreducible background to the Higgs signal in WBF is constituted by Hjj production via gluon fusion (GF). Higgs production via GF is mediated by a heavy quark loop. An exact calculation of $pp \to Hjj$ via GF at the lowest nonvanishing order has been performed in [14]. NLO-QCD calculations have made use of the large top mass limit, where the coupling of the Higgs to gluons is parameterized by an effective vertex [15]. Phenomenological studies have revealed the complementary features of the WBF and the GF Hjj production processes, suggesting search strategies for suppressing the GF channel as background to the clean WBF signature. More recently, GF has also been considered as a signal process [16], because the dijet angular correlation is sensitive to the CP parity of the Higgs boson.

Although GF and WBF are usually considered as separate reactions, their interference in the $qq \to qqH$ subprocesses is possible. In Refs. [17,18] interference effects at tree level due to identical-flavor effects have explicitly been shown to be tiny and entirely negligible for cross sections and distributions. The authors of [18] speculated that loop-induced interference effects should be large. An explicit calculation revealed, however, that loop-induced interference effects are also small [19].

We present a similar calculation for the same process, studying interference effects between GF and WBF which emerge beyond tree level. Being performed with entirely different methods, our work confirms the main findings of Ref. [19] and extends it in two respects: First, we include a class of real emission contributions which has been neglected in [19]. Second, we develop a fully flexible parton-level Monte Carlo program which allows us to study cross sections as well as arbitrary distributions within experimentally feasible selection cuts. Being implemented in the modular VBFNLO environment [20], the impact of the interference contributions on the WBF signal is studied in detail.

We give a thorough outline of our calculation in Sec. II. Numerical results are discussed in Sec. III. We conclude with a brief summary in Sec. IV.

II. ELEMENTS OF THE CALCULATION

A. General framework

Hjj production in WBF mainly proceeds via quark scattering, $qq \to qqH$. In Ref. [17] contributions from

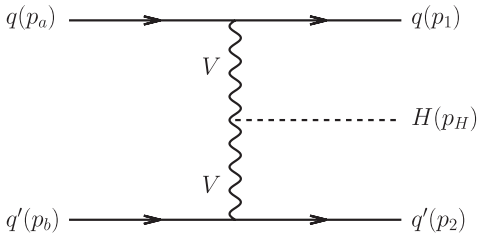

FIG. 1. Feynman diagram for the tree-level process $qq' \to qq'H$ via WBF.

identical-flavor annihilation processes such as $q\bar{q} \to Z^\star \to ZH$ with subsequent decay $Z \to q\bar{q}$ or similar WH production channels have been shown to be entirely negligible in the phase-space regions where WBF can be observed experimentally. In the same work, identical quark interference effects from $qq \to qqH$ and crossing-related channels were demonstrated to affect cross sections and kinematic distributions at an insignificant level. This finding was confirmed by Ref. [18]. In the following we will therefore restrict our discussion to quark scattering via exchange of a weak boson in the t channel, i.e., the reaction $qq' \to qq'H$, where q and q' stand for quarks of different flavor, see Fig. 1. We will refer to the respective tree-level scattering amplitude by $\mathcal{M}^{(0)}_{\mathrm{WBF}}$. Color factors are not included in $\mathcal{M}^{(0)}_{\mathrm{WBF}}$ and will be denoted separately. Adaptation for the crossed processes $q\bar{q}' \to q\bar{q}'H$, $\bar{q}q' \to \bar{q}q'H$, and $\bar{q}\bar{q}' \to \bar{q}\bar{q}'H$ is straightforward.

Higgs production in quark scattering reactions, mediated by a gluon in the t channel which couples to the Higgs boson via a top-quark loop is depicted in Fig. 2(a). For a Higgs mass well below the top-pair production threshold, the coupling of the gluon to a scalar, CP-even Higgs boson can be parameterized by an effective Lagrangian of the form

$$\mathcal{L}_{\mathrm{eff}} = \frac{\alpha_s}{12\pi v} H G^a_{\mu\nu} G^{a\mu\nu}, \tag{2.1}$$

where G denotes the gluonic field tensor and $v = 246$ GeV the vacuum expectation value of the Higgs boson. The respective Feynman diagram is depicted in Fig. 2(b). Throughout this work we will employ this effective coupling for the Hgg vertex. In the following, we denote the lowest order scattering amplitude for $qq' \to qq'H$ via GF by $\mathcal{M}^{(0)}_{\mathrm{GF}}$. Analogous to the WBF case, color factors are not included in the amplitude $\mathcal{M}^{(0)}_{\mathrm{GF}}$.

At tree level, the GF and WBF production channels for $qq' \to qq'H$ do not interfere due to the color structure of the two processes. An interference between GF and the *neutral-current* contributions to WBF becomes possible, however, if an additional gluon emission is considered. Flavor-changing WW-fusion diagrams cannot interfere with the flavor-conserving gluon exchange diagrams. For the neutral-current mode, two types of loop contributions emerge:

(1) One-loop diagrams, where a gluon is exchanged between the upper and the lower fermion line in the WBF diagram of Fig. 1 (for $V = Z$). The respective loop amplitude $\mathcal{M}^{(1\text{-loop})}_{\mathrm{WBF}}$ yields nonvanishing contributions at order $\mathcal{O}(\alpha^2\alpha_s^3)$ when interfering with the tree-level GF production amplitude $\mathcal{M}^{(0)}_{\mathrm{GF}}$. Here, we count the HZZ coupling as αv and the Hgg coupling as α_s/v; see Fig. 3 for a representative Feynman graph.

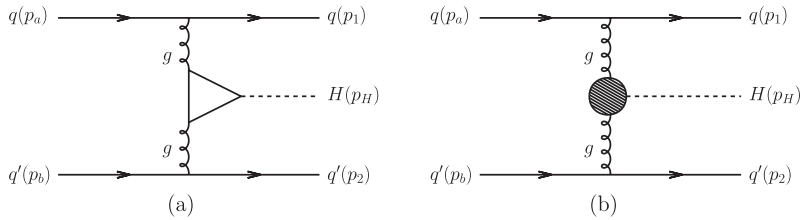

FIG. 2. Feynman diagrams for the tree-level process $qq' \to qq'H$ via GF, mediated (a) by a top-quark loop and (b) by the effective Hgg vertex of Eq. (2.1).

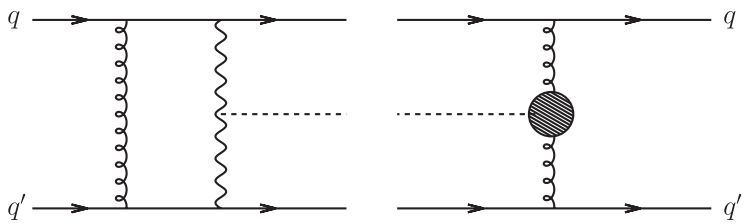

FIG. 3. Representative loop contribution to the interference cross section for $qq' \to qq'H$ via WBF and GF, respectively, at order $\mathcal{O}(\alpha^2\alpha_s^3)$, where the 1-loop WBF amplitude interferes with the tree-level GF amplitude.

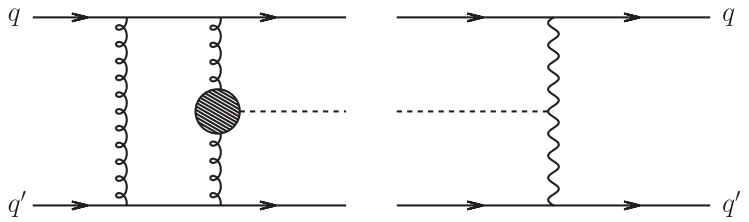

FIG. 4. Representative loop contribution to the interference cross section for $qq' \to qq'H$ via WBF and GF, respectively, at order $\mathcal{O}(\alpha^2\alpha_s^3)$, where the 1-loop GF amplitude interferes with the tree-level WBF amplitude.

(2) GF diagrams with an extra gluon exchanged between the upper and the lower quark line, $\mathcal{M}_{\mathrm{GF}}^{(1\text{-loop})}$. These also contribute at order $\mathcal{O}(\alpha^2\alpha_s^3)$ when interfering with the tree-level ZZ-fusion amplitude $\mathcal{M}_{\mathrm{WBF}}^{(0)}$ as depicted in Fig. 4.

All relevant loop diagrams involve pentagon diagrams. Box, triangle, and bubble diagrams do not contribute due to color conservation.

At the same order in the perturbative expansion, real emission diagrams have to be considered. Nonvanishing neutral-current contributions to the $qq' \to qq'gH$ process arise from the interference of scattering diagrams like those depicted in Fig. 5. The upper diagram shows an interference between gluon emission from the q line in the WBF amplitude and from the q' line in the GF amplitude. In the lower diagram the inverse configuration is illustrated. Interference graphs where both gluons are emitted from the same quark line cancel out when colors are summed over. The same applies to those graphs of the GF amplitude where a gluon is attached to the internal gluon line or to the Hgg vertex. We denote the real emission amplitudes for $qq' \to qq'gH$ that do not cancel by $\mathcal{M}_{\mathrm{WBF}}^{(\mathrm{real})}$ and $\mathcal{M}_{\mathrm{GF}}^{(\mathrm{real,t})}$, respectively. Further contributions to $qq' \to qq'gH$ scattering via GF, referred to as $\mathcal{M}_{\mathrm{GF}}^{(\mathrm{real,f})}$, arise from a topology absent in $qq' \to qq'H$, where the Higgs boson is radiated off the final-state gluon rather than the t-channel exchange boson (see Fig. 6).

Since only diagrams with gluons being emitted from different quark lines contribute to the real emission, no

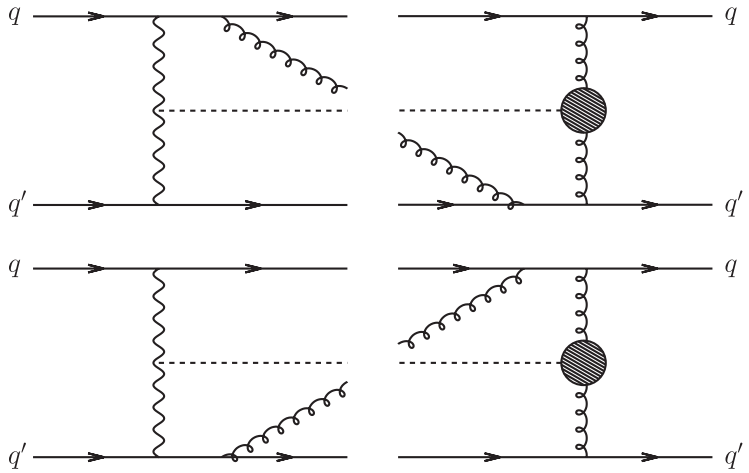

FIG. 5. Representative cut amplitudes for the $qq' \to qq'gH$ process via the interference of WBF and GF amplitudes, at order $\mathcal{O}(\alpha^2\alpha_s^3)$.

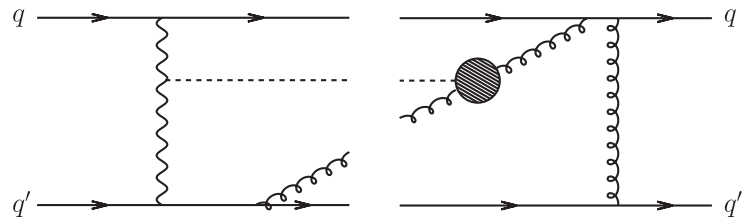

FIG. 6. Representative diagram contributing to the interference of $qq' \to qq'gH$ via WBF and GF, respectively, at order $\mathcal{O}(\alpha^2\alpha_s^3)$.

collinearly divergent configurations emerge. Singularities arise, however, when the final-state gluon in $\mathcal{M}^{(\mathrm{real})}_{\mathrm{WBF}}$ or $\mathcal{M}^{(\mathrm{real,t})}_{\mathrm{GF}}$ is soft. Such divergences in the real emission diagrams are eventually canceled by respective singularities in the virtual contributions. To isolate them in intermediate steps of the calculation, a proper regularization scheme has to be utilized. We therefore perform our calculation in $d = 4 - 2\epsilon$ dimensions, implementing both the dimensional regularization and the dimensional reduction prescriptions [21]. Checking that both schemes yield the same results provides a test of our calculation.

B. Virtual contributions

For the discussion of the loop contributions to Hjj production via WBF and GF, respectively, we resort to the quark-quark scattering process

$$q(p_a) + q'(p_b) \to q(p_1) + q'(p_2) + H(p_H). \tag{2.2}$$

The 1-loop amplitudes we are considering,

$$\mathcal{M}^{(1\text{-loop})}_{\mathrm{WBF}} = \sum_{k=1}^{13} F_k^{\mathrm{WBF}}(p_a, p_1; p_b, p_2)\hat{\mathcal{M}}_k, \tag{2.3}$$

$$\mathcal{M}^{(1\text{-loop})}_{\mathrm{GF}} = \sum_{k=1}^{13} F_k^{\mathrm{GF}}(p_a, p_1; p_b, p_2)\hat{\mathcal{M}}_k, \tag{2.4}$$

can be expressed as linear combinations of process-dependent prefactors, F_k^{WBF} and F_k^{GF}, and fermion spinor chains $\hat{\mathcal{M}}_k$, so-called standard-matrix elements (SME). Following Ref. [22], we introduce

$$\Gamma^{qq}_{\{\alpha,\alpha\beta\gamma\}} = \bar{u}(p_1, \lambda_1)\{\gamma_\alpha, \gamma_\alpha\gamma_\beta\gamma_\gamma\}u(p_a, \lambda_a), \tag{2.5}$$

$$\Gamma^{q'q'}_{\{\alpha,\alpha\beta\gamma\}} = \bar{u}(p_2, \lambda_2)\{\gamma_\alpha, \gamma_\alpha\gamma_\beta\gamma_\gamma\}u(p_b, \lambda_b), \tag{2.6}$$

where $u(p_i, \lambda_i)$ denotes the quark spinor for fermion i with momentum p_i and helicity $\lambda_i = \pm 1/2$. For contractions with an arbitrary momentum p we use the shorthand notation $\Gamma_p \equiv \Gamma_\mu p^\mu$. For the reaction (2.2), 13 SME emerge,

$$\begin{aligned}
\hat{\mathcal{M}}_{\{1,2\}} &= \Gamma^{qq}_{\alpha}\Gamma^{q'q',\{\alpha,\alpha p_1 p_a\}},\\
\hat{\mathcal{M}}_{\{3,4\}} &= \Gamma^{qq}_{\alpha p_2 p_b}\Gamma^{q'q',\{\alpha,\alpha p_1 p_a\}},\\
\hat{\mathcal{M}}_{\{5,6\}} &= \Gamma^{qq}_{p_b}\Gamma^{q'q',\{p_a,p_1\}},\\
\hat{\mathcal{M}}_{\{7,8\}} &= \Gamma^{qq}_{p_2}\Gamma^{q'q',\{p_a,p_1\}},\\
\hat{\mathcal{M}}_{\{9,10\}} &= \Gamma^{qq}_{\alpha\beta p_b}\Gamma^{q'q',\{\alpha\beta p_a,\alpha\beta p_1\}},\\
\hat{\mathcal{M}}_{\{11,12\}} &= \Gamma^{qq}_{\alpha\beta p_2}\Gamma^{q'q',\{\alpha\beta p_a,\alpha\beta p_1\}},\\
\hat{\mathcal{M}}_{13} &= \Gamma^{qq}_{\alpha\beta\gamma}\Gamma^{q'q',\alpha\beta\gamma}.
\end{aligned} \tag{2.7}$$

The SME are computed in two independent ways by means of the helicity amplitude formalism of Ref. [23] and the Weyl–van der Waerden formalism of Ref. [24], respectively.

The coefficients F_k^{WBF} and F_k^{GF} contain coupling factors and remnants of scalar and tensor loop integrals, up to rank two and up to five propagator denominators. For the computation of the tensor coefficients we have employed two different methods and developed two completely independent computer codes. These codes agree with a relative accuracy better than 10^{-8} for nonexceptional phase-space points away from the zeroes of the Gram determinant. The basic features of the two implementations are described in the following.

1. Passarino-Veltman type tensor reduction

In one of our implementations, we have used the conventional Passarino-Veltman (PV) reduction formalism [25,26] for the computation of tensor integrals up to boxes, generalizing the method in a straightforward manner to pentagons in the framework of dimensional regularization. All tensor coefficients are expressed in terms of scalar master integrals in $(4 - 2\epsilon)$ dimensions with a regularization scale μ. Singularities are manifested as single or double poles in ϵ. For GF, only integrals with vanishing internal masses emerge. Expressions for the respective four-point integrals with up to two external off-shell legs are taken from Ref. [27]. The infrared-divergent two- and three-point integrals can be extracted from Refs. [26,28]. For WBF, scalar integrals with up to two massive propagators are needed. We have calculated the divergent box integrals by extracting corresponding expressions in mass regularization from Refs. [29,30]. Employing the method described in Ref. [28] we have transformed these expressions to dimensional regularization (see the Appendix). The remaining finite scalar integrals were calculated with LoopTools [31], and have been compared numerically to the expressions given in Ref. [19].[1]

The double and single pole terms of the coefficients F_k^{WBF} and F_k^{GF} are calculated analytically with the help of MATHEMATICA. To this end, we perform the tensor reduction in two steps: first for the singular pieces in $d = 4 - 2\epsilon$ dimensions, and then in four dimensions for the nonsingular terms. For tensor integrals up to rank two this separation is trivial, since poles do not mix with the finite terms when the reduction formalism is applied. Because of the absence of collinear configurations in the interference process we are focusing on, all double poles present in divergent scalar integrals cancel in the full loop amplitudes. This cancellation occurs for each coefficient F_k^{GF}, $F_k^{\mathrm{WBF}}(k = 1, \ldots, 13)$ separately. The remaining single poles for the GF and WBF contributions are proportional to the respective tree-level amplitudes such that the singular parts of the loop-induced interference contribution take

[1] We identified a misprint in one of the respective expressions of Ref. [19].

the form

$$\begin{aligned}\overline{\sum} 2\,\mathrm{Re}[\mathcal{M}_{\mathrm{WBF}}^{(1\text{-loop})}\mathcal{M}_{\mathrm{GF}}^{(0)\star} + \mathcal{M}_{\mathrm{GF}}^{(1\text{-loop})}\mathcal{M}_{\mathrm{WBF}}^{(0)\star}]_{\mathrm{sing}} \\ = -\frac{\alpha_s}{2\pi}\Gamma(1+\epsilon)\mu^{2\epsilon}\frac{1}{\epsilon}\overline{\sum} 2\,\mathrm{Re}[\mathcal{M}_{\mathrm{WBF}}^{(0)}\mathcal{M}_{\mathrm{GF}}^{(0)\star} \\ + \mathcal{M}_{\mathrm{GF}}^{(0)}\mathcal{M}_{\mathrm{WBF}}^{(0)\star}]\left[\ln\left(\frac{s_{ab}}{4\pi\mu^2}\right) - \ln\left(\frac{-s_{a2}}{4\pi\mu^2}\right)\right. \\ \left. - \ln\left(\frac{-s_{b1}}{4\pi\mu^2}\right) + \ln\left(\frac{s_{12}}{4\pi\mu^2}\right)\right], \qquad (2.8)\end{aligned}$$

where $\overline{\sum}$ denotes averaging over initial-state spin degrees of freedom and summation over final-state ones. Here, we have introduced the notation $s_{ij} = 2p_i \cdot p_j$. We will see below that the divergent pieces are canceled exactly by respective poles in the real emission contributions. In our Monte Carlo program we thus retain only the finite parts of the scalar integrals. The tensor reduction for the nonsingular terms can then be performed numerically.

2. Denner-Dittmaier type tensor reduction

In an independent implementation, we have performed the reduction from five-point to four-point integrals by means of the Denner-Dittmaier (DD) reduction formalism [32], while still reducing the four-point integrals with the conventional PV tensor reduction discussed above. Like the PV method the DD reduction is formulated in d dimensions, but has the advantage of avoiding subtle cancellations, which can spoil the numerical integration. Such cancellations originate from terms with a very small Gram determinant in the denominator. If two or more external momenta are linearly dependent, the Gram determinant vanishes and we encounter numerical instabilities in the respective phase-space regions. In the PV approach, one power of the Gram determinant appears, in general, in each step of the iterative reduction to lower-rank tensors, and also when an N-point function is reduced to $(N-1)$-point integrals. In contrast to the PV reduction, the DD approach avoids Gram determinants in the denominator in the reduction from five-point to four-point integrals. In addition, it reduces the rank of the emerging four-point tensor integrals by one. A similar reduction formalism has also been given in [33].

As expected, the DD method turns out to be numerically far more stable than the PV reduction. Throughout our numerical studies, we will therefore resort to the DD formalism. The PV reduction is used only to test our results.

C. Real emission contributions

For the real emission contribution the partonic subprocess

$$q(p_a) + q'(p_b) \to q(p_1) + q'(p_2) + g(p_g) + H(p_H) \qquad (2.9)$$

has to be considered. The amplitudes $\mathcal{M}_{\mathrm{WBF}}^{(\mathrm{real})}$ and $\mathcal{M}_{\mathrm{GF}}^{(\mathrm{real})} = \mathcal{M}_{\mathrm{GF}}^{(\mathrm{real,t})} + \mathcal{M}_{\mathrm{GF}}^{(\mathrm{real,f})}$ are computed numerically by means of the helicity amplitude formalism of Ref. [23]. Results for $q\bar{q}' \to q\bar{q}'gH$, $\bar{q}q' \to \bar{q}q'gH$, and $\bar{q}\bar{q}' \to \bar{q}\bar{q}'gH$ are obtained analogously. Because of color conservation, crossing-related subprocesses with a gluon in the initial state such as $gq' \to q\bar{q}q'H$ do not contribute to the interference cross section.

To test our implementation we have compared our results for $\mathcal{M}_{\mathrm{WBF}}^{(\mathrm{real})}$ and $\mathcal{M}_{\mathrm{GF}}^{(\mathrm{real})}$ at the amplitude level and for the interference contribution $\overline{\sum} 2\,\mathrm{Re}[\mathcal{M}_{\mathrm{WBF}}^{(\mathrm{real})}\mathcal{M}_{\mathrm{GF}}^{(\mathrm{real})\star} + \mathcal{M}_{\mathrm{GF}}^{(\mathrm{real})}\mathcal{M}_{\mathrm{WBF}}^{(\mathrm{real})\star}]$ to those of MadGraph [34] and found complete agreement within the numerical accuracy of our program.

D. Subtraction procedure

The real emission contributions contain soft divergences which eventually cancel the corresponding poles in the virtual contributions [cf. Eq. (2.8)]. A convenient method for isolating the singularities is the so-called phase-space slicing procedure. It relies on splitting the $qq'gH$ phase space into soft and hard regions by a suitable cutoff parameter and performing the integration of the real emission contributions in the two regimes separately. To check our results we implement two conceptually different slicing methods: the two-cutoff slicing method of Ref. [35] which has been developed in the context of mass regularization, and the phase-space slicing method of Ref. [36] which utilizes a Lorentz-invariant cutoff and dimensional regularization.

1. Lorentz-invariant phase-space slicing

The slicing method of Ref. [36] divides the phase space of the final-state particles into a hard region where all partons can be resolved and an infrared region for soft and collinear configurations. In general, special care is necessary to separate soft and collinear regions in order to avoid double counting of singular configurations. Since the interference contributions of our interest are free of collinear singularities, the formalism can be greatly simplified, however. In the case of $qq' \to qq'gH$ the gluon is considered as infrared when

$$s_{ig} = 2p_i \cdot p_g < s_{\mathrm{min}}, \quad \text{with } i = a, b, 1, 2 \qquad (2.10)$$

for an arbitrarily small cutoff parameter s_{min}, where we closely follow the notation of Ref. [37]. While for collinear configurations only one s_{ig} is small, the soft region is defined by requiring at least two invariants to be smaller than s_{min}. The partonic real emission cross section can then be decomposed into a soft and a hard part,

$$\hat{\sigma}^{\mathrm{real}} = \hat{\sigma}^{\mathrm{soft}} + \hat{\sigma}^{\mathrm{hard}}. \qquad (2.11)$$

The integration over the gluonic degrees of freedom is

performed analytically in $\hat{\sigma}^{\rm soft}$, but purely numerically in $\hat{\sigma}^{\rm hard}$.

In order to calculate $\hat{\sigma}^{\rm soft}$ we use the factorization properties of the real emission amplitude in the soft limit. As the energy of the emitted gluon becomes small, the $qq' \to qq'gH$ interference amplitudes can be approximated by the tree-level interference amplitudes multiplied by a sum of eikonal terms,

$$\begin{aligned}&\overline{\sum} 2\,\mathrm{Re}[\mathcal{M}^{(\rm real)}_{\rm WBF}\mathcal{M}^{(\rm real)\star}_{\rm GF} + \mathcal{M}^{(\rm real)}_{\rm GF}\mathcal{M}^{(\rm real)\star}_{\rm WBF}]_{\rm soft}\\ &= (4\pi\alpha_s)\mu^{2\epsilon}\overline{\sum} 2\,\mathrm{Re}[\mathcal{M}^{(0)}_{\rm WBF}\mathcal{M}^{(0)\star}_{\rm GF} + \mathcal{M}^{(0)}_{\rm GF}\mathcal{M}^{(0)\star}_{\rm WBF}]\\ &\quad\times\left[\frac{2s_{ab}}{s_{ag}s_{bg}} - \frac{2s_{a2}}{s_{ag}s_{2g}} - \frac{2s_{b1}}{s_{bg}s_{1g}} + \frac{2s_{12}}{s_{1g}s_{2g}}\right].\end{aligned} \tag{2.12}$$

The color structure of the soft contribution will be considered below. In the soft region, the four-particle $qq'gH$ phase space factorizes into a three-particle $qq'H$ phase space and the soft gluon phase space for the respective configuration,

$$[d(PS_4)]^{\rm soft} = d(PS_3)d(PS_g)^{\rm soft}(i,j,g), \tag{2.13}$$

where $d(PS_3)$ contains the flux factor, $1/(2\hat{s})$, with $\hat{s}$ denoting the partonic center-of-mass energy squared. For the two outgoing partons i and j, $d(PS_g)^{\rm soft}(i,j,g)$ is given by [36]

$$\begin{aligned}d(PS_g)^{\rm soft}(i,j,g) &= \frac{(4\pi)^\epsilon}{16\pi^2}\frac{s_{ab}^{2\epsilon-1}}{\Gamma(1-\epsilon)}[s_{ig}s_{jg}s_{ij}]^{-\epsilon}ds_{ig}ds_{jg}\\ &\quad\times\theta(s_{\rm min}-s_{ig})\theta(s_{\rm min}-s_{jg}).\end{aligned} \tag{2.14}$$

The integration over the soft gluon phase space can be performed for each term in the soft interference amplitude Eq. (2.12) explicitly, using

$$\begin{aligned}&g_s^2\mu^{2\epsilon}\int d(PS_g)^{\rm soft}(i,j,g)\frac{2s_{ij}}{s_{ig}s_{jg}}\\ &\quad= \frac{g_s^2}{8\pi^2}\frac{1}{\Gamma(1-\epsilon)}\left(\frac{4\pi\mu^2}{s_{\rm min}}\right)^\epsilon\frac{1}{\epsilon^2}\left(\frac{s_{ij}}{s_{\rm min}}\right)^\epsilon.\end{aligned} \tag{2.15}$$

The generalization of this expression to cases where one of the partons i, j is incoming rather than outgoing is straightforward. The soft part of the real emission cross section then takes the form

$$\begin{aligned}\hat{\sigma}^{\rm soft} &= \frac{C_AC_F}{2}\int[d(PS_4)]^{\rm soft}\overline{\sum} 2\,\mathrm{Re}[\mathcal{M}^{(\rm real)}_{\rm WBF}\mathcal{M}^{(\rm real)\star}_{\rm GF} + \mathcal{M}^{(\rm real)}_{\rm GF}\mathcal{M}^{(\rm real)\star}_{\rm WBF}]_{\rm soft}\\ &= \frac{\alpha_s}{2\pi}\Gamma(1+\epsilon)\frac{C_AC_F}{2}\int d(PS_3)\overline{\sum} 2\,\mathrm{Re}[\mathcal{M}^{(0)}_{\rm WBF}\mathcal{M}^{(0)\star}_{\rm GF} + \mathcal{M}^{(0)}_{\rm GF}\mathcal{M}^{(0)\star}_{\rm WBF}]\\ &\quad\times\left\{\left(\frac{1}{\epsilon}+\ln\frac{4\pi\mu^2}{s_{\rm min}}\right)\cdot\left[\ln\left(\frac{s_{ab}}{s_{\rm min}}\right) - \ln\left(-\frac{s_{a2}}{s_{\rm min}}\right) - \ln\left(-\frac{s_{b1}}{s_{\rm min}}\right) + \ln\left(\frac{s_{12}}{s_{\rm min}}\right)\right]\right.\\ &\quad\left.+\frac{1}{2}\left[\ln^2\left(\frac{s_{ab}}{s_{\rm min}}\right) - \ln^2\left(-\frac{s_{a2}}{s_{\rm min}}\right) - \ln^2\left(-\frac{s_{b1}}{s_{\rm min}}\right) + \ln^2\left(\frac{s_{12}}{s_{\rm min}}\right)\right]\right\},\end{aligned} \tag{2.16}$$

where we have included the color factor $C_AC_F/2 = 2$. When $\hat{\sigma}^{\rm soft}$ is combined with the virtual contributions,

$$\hat{\sigma}^{qq'H} = \hat{\sigma}^{\rm virt} + \hat{\sigma}^{\rm soft}, \tag{2.17}$$

all $1/\epsilon$ poles cancel [cf. Eq. (2.8)]. The remaining terms are finite and can be integrated over the three-particle phase space of the $qq'H$ system and convoluted with the parton distributions of the incoming fermions numerically. The resulting three-particle contribution, $\sigma^{qq'H}$, depends on the unphysical cutoff parameter $s_{\rm min}$. This dependence cancels, however, once $\sigma^{qq'H}$ is combined with the hard part of the real emission cross section,

$$\sigma^{\rm full} = \sigma^{\rm hard} + \sigma^{qq'H}. \tag{2.18}$$

Checking that the full NLO interference cross section is independent of the cutoff parameter therefore provides another important test of our calculation.

2. Phase-space slicing with energy cutoff

The phase-space slicing method of Ref. [35] in principle requires two cutoff parameters for separating finite from collinear and soft divergent regions. For our application, however, no collinear singular configurations emerge. Thus, applying a single cutoff on the energy of the potentially soft gluon is sufficient.

In analogy to the Lorentz-invariant slicing method described previously, the real emission contribution can be evaluated numerically in the "hard" region of phase space above the cutoff, where it is completely finite. Below the energy cutoff, however, the phase-space integration over the gluonic degrees of freedom is performed analytically. Following Refs. [38,39], this "soft" contribution to the partonic cross section can be written as

$$\hat{\sigma}^{\text{soft},E\text{-cut}} = \frac{\alpha_s}{2\pi}\frac{C_A C_F}{2}\int d(PS_3)\overline{\sum} 2\,\text{Re}[\mathcal{M}^{(0)}_{\text{WBF}}\mathcal{M}^{(0)\star}_{\text{GF}} + \mathcal{M}^{(0)}_{\text{GF}}\mathcal{M}^{(0)\star}_{\text{WBF}}] \times \int_{|\mathbf{p_g}|^2=E_3^2-\lambda^2}^{E_3<\Delta E} \frac{d^3\mathbf{p_g}}{2\pi E_3}\left[\frac{2s_{ab}}{s_{ag}s_{bg}} - \frac{2s_{a2}}{s_{ag}s_{2g}} - \frac{2s_{b1}}{s_{bg}s_{1g}} + \frac{2s_{12}}{s_{1g}s_{2g}}\right], \tag{2.19}$$

where E_3 is the gluon energy, ΔE the energy cutoff in the rest frame of the two incoming partons, and λ a mass used as regulator. As above, $d(PS_3)$ denotes the $qq'H$ phase space. Evaluating the integrals over the gluonic degrees of freedom in Eq. (2.19) and rewriting the mass-regulated result in terms of dimensional regularization, the corresponding soft cross section is of the form

$$\begin{aligned}\hat{\sigma}^{\text{soft},E\text{-cut}} = \frac{\alpha_s}{2\pi}\frac{C_A C_F}{2}\int d(PS_3)\overline{\sum} 2\,\text{Re}[\mathcal{M}^{(0)}_{\text{WBF}}\mathcal{M}^{(0)\star}_{\text{GF}} + \mathcal{M}^{(0)}_{\text{GF}}\mathcal{M}^{(0)\star}_{\text{WBF}}] \\ \times\left\{\frac{\Gamma(1+\epsilon)}{\epsilon}\left(\frac{\pi\mu^2}{\Delta E^2}\right)^{\epsilon}\left[\ln\left(\frac{s_{ab}}{4\pi\mu^2}\right) - \ln\left(\frac{-s_{a2}}{4\pi\mu^2}\right) - \ln\left(\frac{-s_{b1}}{4\pi\mu^2}\right) + \ln\left(\frac{s_{12}}{4\pi\mu^2}\right)\right]\right. \\ \left. + \text{Li}_2\left(1-\frac{4E_aE_b}{s_{ab}}\right) - \text{Li}_2\left(1-\frac{4E_aE_2}{s_{a2}}\right) - \text{Li}_2\left(1-\frac{4E_bE_1}{s_{b1}}\right) + \text{Li}_2\left(1-\frac{4E_1E_2}{s_{12}}\right)\right\},\end{aligned} \tag{2.20}$$

where the E_i denote the quark energies in the partonic rest frame. In complete analogy to the Lorentz-invariant phase-space slicing, the soft contribution to the partonic cross section is combined with the virtual cross section. The resulting sum is then free of soft poles and can be evaluated numerically. Upon adding the hard part of the real emission contribution, the dependence on the cutoff parameter ΔE cancels.

3. Checks

We have checked that the total $pp \to Hjj$ interference cross section at the LHC within typical WBF cuts (for details, see our standard definition of cuts in Sec. III) is independent of the cutoff parameter for both phase-space slicing schemes.

For the Lorentz-invariant slicing method, we have varied s_{min} in the range $1\ \text{GeV}^2 < s_{\text{min}} < 10^3\ \text{GeV}^2$. For smaller cutoff values, large logarithms arise and numerical instabilities are to be expected. If, on the other hand, a very large value is chosen for s_{min}, the soft approximation used for determining $\hat{\sigma}^{\text{soft}}$ is not applicable anymore. Figure 7(a) demonstrates that the two contributions $\sigma^{qq'H}$ and σ^{hard} individually depend on s_{min}, while the sum σ^{full} is constant in the considered range of the cutoff parameter.

A very similar pattern arises for the energy-cutoff slicing method, depicted in Fig. 7(b). We have normalized the energy cutoff ΔE by $\sqrt{\hat{s}}$ for this study.

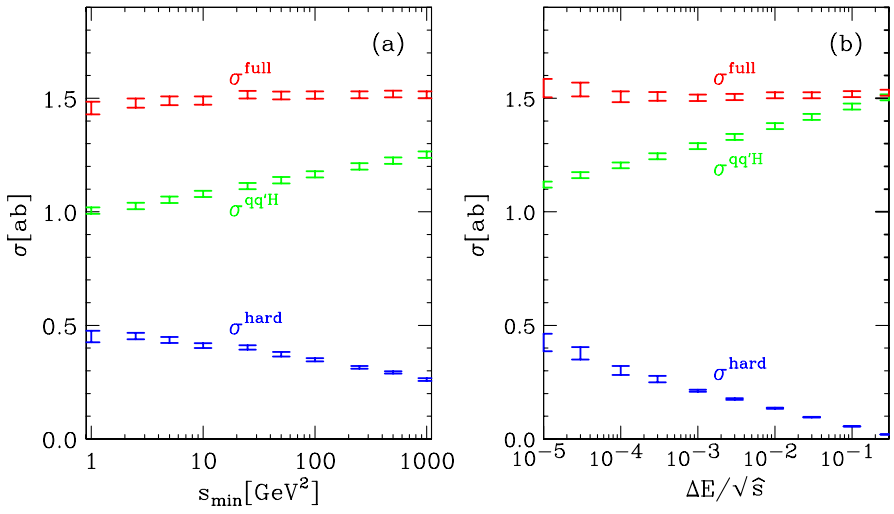

FIG. 7 (color online). Dependence of the interference cross section for $pp \to Hjj$ production at the LHC within standard selection cuts on the cutoff of the Lorentz-invariant phase-space slicing method (a) and of the energy-cutoff slicing method (b). Shown are σ^{hard} (blue), $\sigma^{qq'H}$ (green), and their sum, σ^{full} (red).

III. NUMERICAL RESULTS

The cross section contributions discussed above have been implemented in a fully flexible parton-level Monte Carlo program, structured analogous to the VBFNLO code [20] which has been developed for the study of WBF-type production processes at the LHC.

The loop-induced interference contributions for Hjj production via GF and WBF we consider are a gauge-invariant subclass of the full NLO-QCD corrections to the scattering process $pp \to Hjj$. For the parton distribution functions of the proton we therefore use the CTEQ6M set at NLO [40] with $\alpha_s(m_Z) = 0.118$. We set quark masses to zero throughout and neglect contributions from external top or bottom quarks. As electroweak input parameters we have chosen the gauge boson masses, $m_Z = 91.188$ GeV, $m_W = 80.419$ GeV, and the measured value of the Fermi constant, $G_F = 1.166 \times 10^{-5}/\text{GeV}^2$. Thereof, we compute $\sin^2\theta_W$ and α using LO electroweak relations. For reconstructing jets from final-state partons, we use the k_T algorithm [41] with resolution parameter $R^{k_T} = 0.8$.

Since we want to study the impact of the interference contributions on the Higgs signal in WBF, we apply cuts that are typical for WBF studies at the LHC. We require at least two hard jets with

$$p_{Tj} \geq 20 \text{ GeV}, \qquad |y_j| \leq 4.5, \tag{3.1}$$

where p_{Tj} is the transverse component and y_j the rapidity of the (massive) jet momentum which is reconstructed as the four-vector sum of massless partons of pseudorapidity $|\eta| < 5$. We refer to the two reconstructed jets of highest transverse momentum as ''tagging jets''. The Higgs boson decay products, which we generically call ''leptons'' in the following, are required to be located between the two tagging jets, and they should be well observable. To simulate a generic Higgs decay without specifying a particular channel we generate an isotropic Higgs boson decay into two massless particles (which represent $\gamma\gamma$ or $b\bar{b}$ final states) and require

$$p_{T\ell} \geq 20 \text{ GeV}, \qquad |\eta_\ell| \leq 2.5, \qquad \Delta R_{j\ell} \geq 0.6, \tag{3.2}$$

where $\Delta R_{j\ell}$ denotes the jet-lepton separation in the rapidity-azimuthal angle plane. In addition, the leptons need to fall between the rapidities of the two tagging jets

$$y_{j,\min} < \eta_\ell < y_{j,\max}. \tag{3.3}$$

Furthermore, we impose large rapidity separation of the two tagging jets,

$$\Delta y_{jj} = |y_{j1} - y_{j2}| > 4, \tag{3.4}$$

and demand that the two tagging jets be located in opposite detector hemispheres,

$$y_{j1} \times y_{j2} < 0, \tag{3.5}$$

with an invariant mass

$$M_{jj} > 600 \text{ GeV}. \tag{3.6}$$

To ensure the reliability of our calculation, we have compared our results to those of Ref. [19] and found agreement with their main predictions. Diagrams where the Higgs boson is radiated off the final-state gluon rather than the t-channel exchange boson as in Fig. 6 have not been considered in [19]. This approximation seems reasonable, as we found that contributions from these graphs amount to only about 0.3% of the total interference cross section. For individual subprocesses they can be larger, however. For the $dd \to ddH$ channel, for instance, they yield approximately 5% of the subprocess cross section.

In Fig. 8 we show the total cross section $\sigma_{\text{int}}^{\text{cuts}}$ for the interference contribution within the cuts of Eqs. (3.1), (3.2), (3.3), (3.4), (3.5), and (3.6) and for a Higgs mass of $m_H = 120$ GeV. The factorization scale, μ_f, and the renormalization scale, μ_r, which enters the strong coupling, are chosen as follows: In panel (a), we set

$$\mu_f = \xi_f m_H, \qquad \alpha_s^3(\mu_r) = \alpha_s^3(\xi_r m_H). \tag{3.7}$$

In panel (b), we associate the scale for gluon emission from either quark line with the transverse momentum of the corresponding jet by setting

$$\begin{aligned} \mu_f &= \xi_f p_{Tj}, \\ \alpha_s^3(\mu_r) &= \alpha_s(\xi_r p_{T1}) \cdot \alpha_s(\xi_r p_{T2}) \cdot \alpha_s(\xi_r m_H). \end{aligned} \tag{3.8}$$

Because of the absence of collinear singularities, μ_f enters only via the parton distribution functions of the incoming fermions, which are mainly probed at rather large values of Feynman x. In this regime, the valence and sea quark distributions depend on the factorization scale only mildly. Thus, the variation of $\sigma_{\text{int}}^{\text{cuts}}$ with μ_f is very small. On the other hand, the interference cross section exhibits a pronounced dependence on μ_r. Since the loop-induced GF $\times$ WBF interference in $qq' \to qq'H$ production, $\sigma_{\text{int}}^{\text{cuts}}$, represents the first nonvanishing contribution in the perturbative expansion, the renormalization scale enters only via the strong coupling constant. Thus, the entire μ_r dependence of the interference cross section can be traced back to the variation of the $\alpha_s^3(\mu_r)$ coupling factor with the renormalization scale. Reminiscent of what has been observed for pure WBF production processes (cf., e.g., Ref. [42]), a dynamical scale choice as in Eq. (3.8) [see Fig. 8(b)] yields predictions with a somewhat reduced scale dependence as compared to the fixed scale option of Eq. (3.7), shown in Fig. 8(a).

Compared to the total WBF cross section within typical selection cuts, the interference contribution we have calculated is almost negligible in magnitude. In Table I we list σ^{cuts} for both, interference and pure WBF cross sections for the various flavor combinations of the scattering quarks

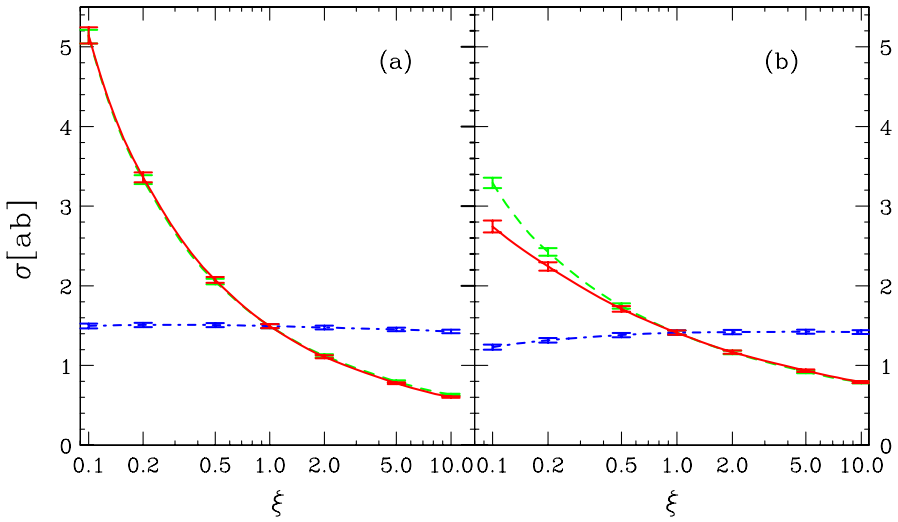

FIG. 8 (color online). Dependence of the total interference cross section $\sigma_{\rm int}^{\rm cuts}$ for Hjj production at the LHC on the factorization and renormalization scales for the two different scenarios described in the text. The factorization scale $\mu_{\rm f}$ and the renormalization scale $\mu_{\rm r}$ are scaled as m_H for (a) and as the jets' transverse momenta in (b); cf. Eqs. (3.7) and (3.8), respectively. The curves show $\sigma_{\rm int}^{\rm cuts}$ as a function of the scale parameter ξ for three different cases: $\xi_{\rm r} = \xi_{\rm f} = \xi$ (red solid line), $\xi_{\rm f} = \xi$ and $\xi_{\rm r} = 1.0$ (blue dash-dotted line), $\xi_{\rm r} = \xi$ and $\xi_{\rm f} = 1.0$ (green dashed line).

and antiquarks, setting $\mu_{\rm f} = \mu_{\rm r} = m_H$. For WBF, we consider neutral- and charged-current subprocesses at $\mathcal{O}(\alpha^3)$. No W-exchange diagrams contribute to the interference cross section. Table I reveals the strong cancellations occurring in $\sigma_{\rm int}^{\rm cuts}$ among the separate channels. While some contributions, in particular, for the qq' subprocesses, are sizeable, their sum amounts to 1.5 ab only. We will show below that the subtle cancellation between the same and opposite isospin qq, $q\bar{q}$, and $\bar{q}\,\bar{q}$ scattering contributions leads to unexpected shapes of kinematic distributions in flavor-blind experiments.

Figure 9 depicts the shapes of the transverse-momentum distributions for "pure" WBF Hjj production and for the WBF $\times$ GF interference contribution we have calculated. The very hard $p_{\rm T}$ distribution encountered for the interference significantly differs from the shape of the WBF curve. The small size of the $p_{\rm T}$ distribution at low momentum transfer is mainly due to strong cancellations among the different flavor contributions to the full $pp \to Hjj$ interference cross section, as illustrated by Fig. 9(b), where the contributions for same isospin and opposite isospin $qq + q\bar{q} + \bar{q}\,\bar{q}$ scattering, $\sigma_{\rm int}^{\rm pos}$ and $\sigma_{\rm int}^{\rm neg}$, are shown separately. The two contributions cancel almost precisely to give the total interference contribution, $\sigma_{\rm int}^{\rm pos} + \sigma_{\rm int}^{\rm neg} = \sigma_{\rm int}$. At high $p_{\rm T}$, the cancellation effects are less pronounced. In short, the interference contribution has a harder transverse-momentum spectrum than expected, because of a very efficient cancellation around $p_{\rm T,tag}^{\rm max} \sim 100$ GeV, where the individual distributions peak.

This cancellation pattern is reflected by the tagging-jet invariant mass M_{jj}. For studying the corresponding shapes of the pure EW and of the mixed QCD-EW production processes, we have switched off the invariant-mass cut of Eq. (3.6). The emerging curves are displayed in Fig. 10. While the interference cross section is negative at small values of the dijet-invariant mass, it is relatively large at high M_{jj}. Indeed, it is remarkable to find that the interference cross section yields an even harder M_{jj} distribution than the pure WBF cross section does. This behavior is somewhat unexpected if considering the rather soft invariant-mass distribution of the pure GF Hjj production process which has been reported in the literature [14]. The full GF $pp \to Hjj$ cross section, however, is dominated by gluon-initiated partonic channels such as $gg \to ggH$ and $qg \to qgH$. To the interference cross section, on the other

TABLE I. Contributions of various neutral-current (NC) flavor combinations to $\sigma_{\rm int}^{\rm cuts}$ (in ab) and $\sigma_{\rm WBF}^{\rm cuts}$ (in fb), and of the charged-current (CC) contributions to WBF. Also shown is their sum within the cuts of Eqs. (3.1), (3.2), (3.3), (3.4), (3.5), and (3.6).

Initial-state flavor combination	$\sigma_{\rm int}^{\rm cuts}$ [ab]	$\sigma_{\rm WBF}^{\rm cuts}$ [fb]
NC: $(u+c)(u+c) + (d+s)(d+s)$	51.4	72.3
NC: $(u+c)(d+s)$	−49.8	70.8
CC: $(u+c)(d+s)$		405.7
NC: $(u+c)(\bar{u}+\bar{c}) + (d+s)(\bar{d}+\bar{s})$	−3.1	39.3
NC: $(u+c)(\bar{d}+\bar{s}) + (\bar{u}+\bar{c})(d+s)$	2.2	43.0
CC: $(u+c)(\bar{u}+\bar{c}) + (d+s)(\bar{d}+\bar{s})$		230.7
NC: $(\bar{u}+\bar{c})(\bar{u}+\bar{c}) + (\bar{d}+\bar{s})(\bar{d}+\bar{s})$	4.0	5.1
NC: $(\bar{u}+\bar{c})(\bar{d}+\bar{s})$	−3.2	4.3
CC: $(\bar{u}+\bar{c})(\bar{d}+\bar{s})$		25.7
Sum	1.5	896.9

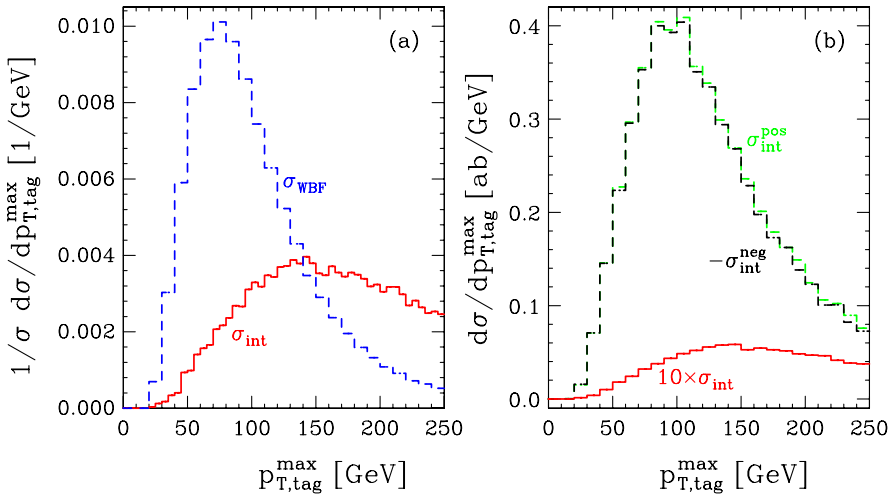

FIG. 9 (color online). Panel (a) shows the normalized transverse-momentum distributions for the tagging jet with the highest p_T for WBF (blue dashed line) and for the WBF $\times$ GF interference contribution (red solid line). In panel (b) the sum of all positive (green dashed line) and the magnitude of all negative contributions (black dashed line) are shown separately. The red solid line gives the sum of all contributions, multiplied by a factor of 10.

hand, only quark (and antiquark) initiated subprocesses contribute, which tend to give larger values of M_{jj} than gluonic contributions. More importantly, the cancellation effects reported above in the context of the tagging-jet transverse-momentum distribution affect the summation over the various flavor contributions to the dijet-invariant-mass distribution in a similar manner, thereby giving rise to a broad invariant-mass distribution which is very small at low values of M_{jj}.

The aforementioned cancellations have different effects on the rapidity distribution of the third, nontagged jet with respect to the tagged jet located in the positive-rapidity hemisphere,

$$y_{diff} = y_3 - \max(y_1, y_2), \tag{3.9}$$

which is shown in Fig. 11 for the interference contribution and the pure WBF cross section. The separation of the lowest p_T jet from the tagged jet located in the negative-rapidity hemisphere, $-y_3 + \min(y_1, y_2)$, would be a mirror copy thereof due to our symmetric selection cuts. For generating the distribution, we required a minimum transverse momentum of $p_{T3} \geq 10$ GeV for the third jet in addition to the selection cuts of Eqs. (3.1), (3.2), (3.3), (3.4), (3.5), and (3.6). The peak of the distribution at small $|y_{diff}|$ emphasizes that the soft jet prefers being close in rapidity to the hard jet in the respective detector hemi-

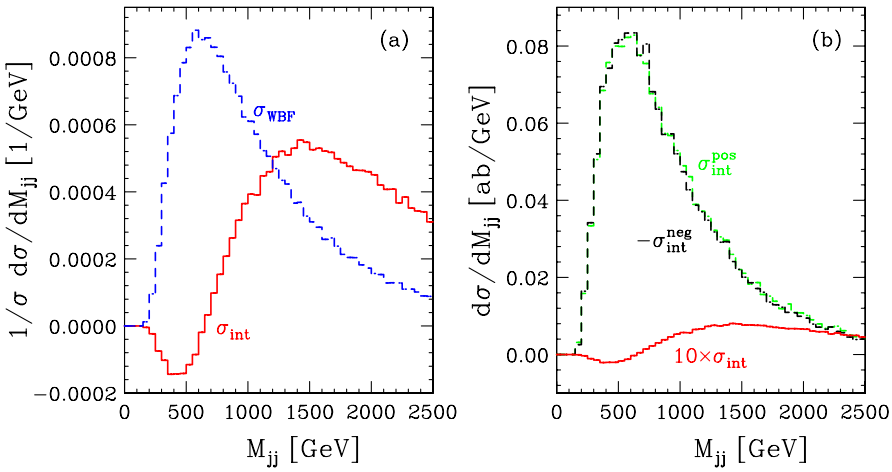

FIG. 10 (color online). Panel (a) shows the normalized tagging-jet invariant-mass distributions for WBF (blue dashed line) and for the WBF $\times$ GF interference contribution (red solid line). Panel (b) depicts the sum of all positive contributions, σ_{int}^{pos} (green dashed line), the magnitude of all negative contributions, $-\sigma_{int}^{neg}$ (black dashed line), and their sum, σ_{int}, multiplied by a factor of 10 (red solid line).

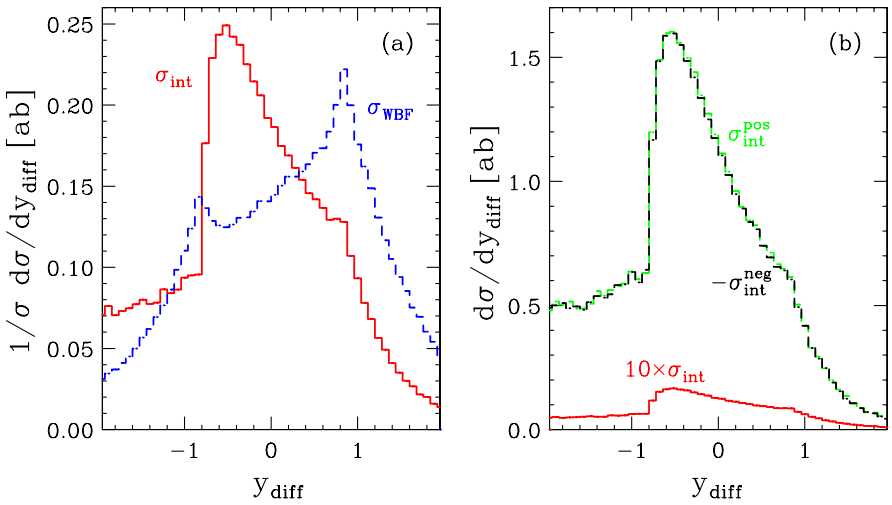

FIG. 11 (color online). Panel (a) shows the normalized rapidity-separation distribution of the nontagged jet for WBF (blue dashed line) and for the WBF $\times$ GF interference contribution (red solid line). Panel (b) depicts the sum of all positive contributions, $\sigma_{\rm int}^{\rm pos}$ (green dashed line), the magnitude of all negative contributions, $-\sigma_{\rm int}^{\rm neg}$ (black dashed line), and their sum, $\sigma_{\rm int}$, multiplied by a factor of 10 (red solid line).

sphere for both, interference and WBF contributions. While in WBF the third jet prefers rapidities larger than the associated tag jet, $y_{\rm diff} > 0$, for the interference contribution $y_{\rm diff}$ peaks at negative values for the various flavor contributions and their sum, indicating that the soft jet is typically located in *between* the two tagged jets. This may indicate that the rapidity gap for a color singlet EW-boson exchange may in general be filled by the EW-QCD interference contribution.

IV. SUMMARY AND CONCLUSIONS

In this article we have computed the order $\mathcal{O}(\alpha^2\alpha_s^3)$ interference contributions to the Hjj production cross section in pp collisions at the LHC via GF and WBF. Since results for the total interference cross section and angular distributions have already been discussed in the literature [19], we have put special emphasis on technical and phenomenological aspects of the calculation which have not been discussed elsewhere. In particular, we have given a detailed outline of the methods used for the evaluation of loop contributions, the subtraction of singularities present in intermediate steps of the calculation, and the checks we have performed to ensure the reliability of our results. In the real emission contributions we have included a finite class of diagrams that has not been considered previously. We found the numerical value of these contributions small, however.

Having implemented the interference amplitudes in a flexible Monte Carlo program based on the VBFNLO framework of Ref. [20], we are able to provide total cross sections and arbitrary kinematic distributions within experimentally feasible selection cuts. Considering the interference cross section as possible ''contamination'' of the clean WBF Hjj production signature, we have studied the associated contributions within typical WBF cuts with widely separated hard tag jets and compared the shape of some characteristic distributions to those of the respective pure WBF curves. We found that, indeed, the interference contributions exhibit features rather different from the WBF signal which are caused by strong cancellations among the separate flavor channels. However, due to the small size of the interference cross section which is found to be in the atto-barn range only, the impact of this contribution to both, integrated cross sections and differential distributions, is negligible.

ACKNOWLEDGMENTS

We are grateful to Stefan Dittmaier and Dieter Zeppenfeld for helpful comments. A. B. would like to thank Junpei Fujimoto and Yoshimasa Kurihara for useful discussions. Our work was supported by the Japan Society for the Promotion of Science, the Deutsche Forschungsgemeinschaft , and partly by the Grant-in-Aid for Scientific Research (No. 17540281) from MEXT, Japan.

APPENDIX: INFRARED-DIVERGENT SCALAR BOX INTEGRALS

In this appendix, we denote the infrared-divergent box integrals with massive propagators which emerge in the calculation of the loop corrections to WBF-induced pentagon diagrams. We do not list the other scalar loop integrals encountered in our calculation, since they can be found elsewhere (see, e.g., [19,27,31]).

We obtained the respective soft and collinear singular box diagrams by extracting appropriate expressions from Refs. [29,30] in the limit of small quark masses. According

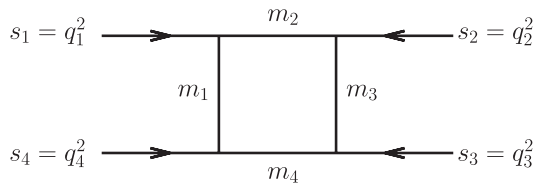

FIG. 12. Momentum and mass assignments for a general scalar box diagram.

to Ref. [28], a relation between different regularization schemes can be established making use of the genuine singularity structure of infrared-divergent triangle integrals. With the help of this property, we transformed the divergent four-point integrals from mass regularization to dimensional regularization.

In the following, we refer to a genuine scalar four-point function as depicted in Fig. 12,

$$\begin{aligned} D_0(q_1, q_2, q_3; m_1, m_2, m_3, m_4) &= \frac{(2\pi\mu)^{4-d}}{(i\pi^2)} \int d^d q \frac{1}{[q^2 - m_1^2 + i\delta][(q+q_1)^2 - m_2^2 + i\delta]} \\ &\quad \times \frac{1}{[(q+q_1+q_2)^2 - m_3^2 + i\delta][(q+q_1+q_2+q_3)^2 - m_4^2 + i\delta]} \\ &\equiv I_4^d(s_1, s_2, s_3, s_4; s_{12}, s_{23}; m_1^2, m_2^2, m_3^2, m_4^2), \end{aligned} \tag{A1}$$

where the q_i denote incoming momenta of the external legs and the m_i correspond to the masses of the internally propagating particles. The kinematic invariants, s_i and s_{ij}, are related to the external momenta via $s_i = q_i^2$ and $s_{ij} = (q_i + q_j)^2$. Overlined quantities are defined as $\bar{s} = s + i\delta$, etc.

In this notation, the collinear divergent box integral with two equal internal and two different external mass scales, which is sketched in Fig. 13, takes the form

$$\begin{aligned} I_4^d(m_H^2, 0, 0, s_4; s, t; m^2, m^2, 0, 0) &= \frac{1}{D_1}\Bigg\{\frac{\Gamma(1+\epsilon)}{\epsilon}\left(\frac{4\pi\mu^2}{m^2}\right)^{\epsilon}\left[\ln\left(\frac{m^2 - \bar{s}_4}{m^2 - \bar{s}}\right) + \ln\left(\frac{m^2}{m^2 - \bar{t}}\right)\right] - \frac{1}{2}\ln^2\left(\frac{-D_1}{m^2(m^2 - s_4)}(1 + i\delta)\right) \\ &\quad + \frac{1}{2}\ln^2(-x_{14}k_1) + \frac{1}{2}\ln^2\left(-\frac{x_{14}}{k_1}\right) - \frac{1}{2}\ln^2(-k_2 x_{14}) - 2\pi i\theta\left(\frac{(m^2 - s)(m^2 - s_4)}{D_1}\right) \\ &\quad \times\left[\theta\left(\frac{m_H^2 - 2m^2}{m^2}\right)\ln(x_{14}k_1) + \theta\left(\frac{2m^2 - m_H^2}{m^2}\right)\ln\left(\frac{x_{14}}{k_1}\right) - \theta\left(\frac{s_4 - t}{m^2}\right)\ln(k_2 x_{14})\right] \\ &\quad - 2\pi i\theta\left(\frac{s - m^2}{m^2}\right)\theta\left(\frac{m^2(m^2 - s_4)}{D_1}\right)\left[\ln\left(\frac{D_1(m^2 - s)}{m^2(m^2 - s_4)^2}(1 + i\delta)\right) + \ln\left(\frac{m^2 - t}{m^2} - i\delta\right)\right] \\ &\quad - \frac{\pi^2}{6} + 2\mathrm{Li}_2\left(\frac{\bar{s} - \bar{s}_4}{m^2 - \bar{s}_4}\right) - 2\mathrm{Li}_2\left(\frac{-\bar{t}}{m^2 - \bar{t}}\right) + \mathrm{Li}_2\left(1 + \frac{D_1}{m^2(m^2 - s_4)}(1 + i\delta)\right) \\ &\quad - \mathrm{Li}_2\left(1 + \frac{D_2}{D_1(m^2 - s)} - i\delta\frac{m^2(m^2 - s_4)}{D_1}\right) + \mathrm{Li}_2\left(1 + \frac{x_{24}}{k_1}\right) + \eta\left(-x_{24}, \frac{1}{k_1}\right)\ln\left(1 + \frac{x_{24}}{k_1}\right) \\ &\quad + \mathrm{Li}_2(1 + x_{24}k_1) + \eta(-x_{24}, k_1)\ln(1 + x_{24}k_1) - \mathrm{Li}_2(1 + x_{24}k_2) \\ &\quad - \eta(-x_{24}, k_2)\ln(1 + x_{24}k_2) + 2\pi i\theta\left(\frac{s - m^2}{m^2}\right)\theta\left(\frac{m^2(s_4 - m^2)}{D_1}\right) \\ &\quad \times\left[\ln\left(\frac{(m_H^2(m^2 - s) + s^2)m^2}{D_1(m^2 - s)} - i\delta\frac{m^2(m^2 - s)}{D_1}\right) + \ln\left(\frac{m^2 - t}{m^2} - i\delta\right)\right]\Bigg\}, \end{aligned} \tag{A2}$$

with

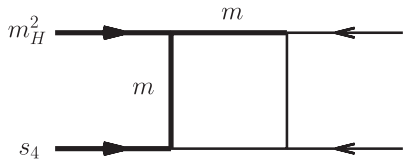

FIG. 13. Momentum and mass assignments for the collinear divergent scalar box diagram of Eq. (A2). Unlabeled thin lines correspond to massless particles.

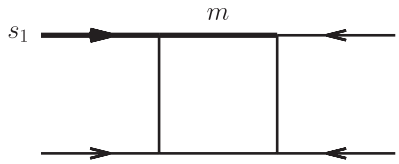

FIG. 14. Momentum and mass assignments for the soft divergent scalar box diagram of Eq. (A4). Unlabeled thin lines correspond to massless particles.

$$
\begin{aligned}
\eta(a,b) &= \ln(ab) - \ln(a) - \ln(b),\\
D_1 &= (s-m^2)(t-m^2) + (s_4-m^2)m^2,\\
D_2 &= m_H^2(m^2-s)(m^2-t) + m^2[m^2(s+t-s_4) + s(s_4-2t)],\\
\beta &= \sqrt{1-4\frac{m^2}{m_H^2} + 2i\delta\frac{m^2}{m_H^4}(m_H^2-2m^2)\theta(4m^2-m_H^2)},\\
x_{14} &= \frac{D_1(m^2-s)}{m^4(m^2-s_4)},\\
x_{24} &= \frac{D_2}{D_1 m_2} - i\delta\frac{(m^2-s)(m^2-s_4)}{D_1},\\
k_1 &= \frac{2m^2-(1+\beta)m_H^2}{2m^2} + i\delta\frac{2m^2-(1+\beta)m_H^2}{2\beta m_H^2},\\
k_2 &= \frac{m^2-s_4}{m^2-t} + i\delta\frac{m^2(t-s_4)}{(m^2-t)^2}.
\end{aligned}
\tag{A3}
$$

The soft divergent box integral with one internal and one external mass scale shown in Fig. 14 is given by

$$
\begin{aligned}
I_4^d(s_1,0,0,0;s,t;0,m^2,0,0) = \frac{1}{s(t-m^2)}\Bigg\{&\frac{\Gamma(1+\epsilon)}{\epsilon^2}\left(\frac{4\pi\mu^2}{-\bar{s}}\right)^{\epsilon} + \frac{\Gamma(1+\epsilon)}{\epsilon}\left(\frac{4\pi\mu^2}{m^2}\right)^{\epsilon}\left[\ln\left(\frac{m^2-\bar{s}_1}{m^2-\bar{t}}\right) + \ln\left(\frac{m^2}{m^2-\bar{t}}\right)\right]\\
&- \frac{1}{2}\ln^2\left(-\frac{\bar{s}}{m^2}\right) - 2\ln\left(-\frac{\bar{s}}{m^2}\right)\ln\left(\frac{m^2}{m^2-\bar{t}}\right) - \ln^2\left(\frac{m^2-\bar{s}_1}{m^2}\right) + \mathrm{Li}_2\left(\frac{\bar{s}_1-m^2}{\bar{s}}\right)\\
&- 2\mathrm{Li}_2\left(\frac{\bar{s}_1-\bar{t}}{m^2-\bar{t}}\right) - 2\mathrm{Li}_2\left(\frac{-\bar{t}}{m^2-\bar{t}}\right) - \ln\left(\frac{\bar{s}}{\bar{s}_1-m^2}\right)\ln\left(1-\frac{\bar{s}_1-m^2}{\bar{s}}\right) - \frac{\pi^2}{2}\Bigg\}.
\end{aligned}
\tag{A4}
$$

We would like to note that our results agree with those of Ref. [19], if μ^2 is replaced by μ in all terms of Eq. (A.19) in [19].

[1] ATLAS Collaboration, ATLAS TDR, Report No. CERN/LHCC/99-15, 1999; G. L. Bayatian *et al.* (CMS Collaboration), J. Phys. G **34**, 995 (2007).

[2] D. Rainwater and D. Zeppenfeld, Phys. Rev. D **60**, 113004 (1999); **61**, 099901(E) (2000); N. Kauer, T. Plehn, D. Rainwater, and D. Zeppenfeld, Phys. Lett. B **503**, 113 (2001).

[3] D. Zeppenfeld, R. Kinnunen, A. Nikitenko, and E. Richter-Was, Phys. Rev. D **62**, 013009 (2000); T. Plehn, D. Rainwater, and D. Zeppenfeld, Phys. Rev. Lett. **88**, 051801 (2002); M. Dührssen *et al.*, Phys. Rev. D **70**, 113009 (2004).

[4] T. Han, G. Valencia, and S. Willenbrock, Phys. Rev. Lett. **69**, 3274 (1992).

[5] T. Figy, C. Oleari, and D. Zeppenfeld, Phys. Rev. D **68**, 073005 (2003); E. L. Berger and J. Campbell, Phys. Rev. D **70**, 073011 (2004).

[6] C. Oleari and D. Zeppenfeld, Phys. Rev. D **69**, 093004 (2004).

[7] B. Jäger, C. Oleari, and D. Zeppenfeld, J. High Energy Phys. 07 (2006) 015; Phys. Rev. D **73**, 113006 (2006).

[8] P. Nason, S. Dawson, and R. K. Ellis, Nucl. Phys. **B303**, 607 (1988).

[9] S. Dittmaier, P. Uwer, and S. Weinzierl, Phys. Rev. Lett.

98, 262002 (2007).
[10] V. Hankele, G. Klämke, D. Zeppenfeld, and T. Figy, Phys. Rev. D **74**, 095001 (2006).
[11] A. Djouadi and M. Spira, Phys. Rev. D **62**, 014004 (2000).
[12] M. Ciccolini, A. Denner, and S. Dittmaier, Phys. Rev. D **77**, 013002 (2008).
[13] M. M. Weber, Nucl. Phys. B, Proc. Suppl. **160**, 200 (2006); arXiv:0709.2668; R. Harlander, J. Vollinga, and M. Weber, arXiv:0801.3355.
[14] V. Del Duca *et al.*, Phys. Rev. Lett. **87**, 122001 (2001); Nucl. Phys. **B616**, 367 (2001).
[15] J. M. Campbell, R. K. Ellis, and G. Zanderighi, J. High Energy Phys. 10 (2006) 028.
[16] G. Klämke and D. Zeppenfeld, J. High Energy Phys. 04 (2007) 052.
[17] C. Georg, diploma thesis, Universität Karlsruhe, 2005, http://www-itp.physik.uni-karlsruhe.de/diplomatheses.de.shtml.
[18] J. R. Andersen and J. M. Smillie, Phys. Rev. D **75**, 037301 (2007).
[19] J. R. Andersen, T. Binoth, G. Heinrich, and J. M. Smillie, arXiv:0709.3513.
[20] M. Bähr *et al.*, http://www-itp.particle.uni-karlsruhe.de/~vbfnloweb/.
[21] W. Siegel, Phys. Lett. B **84**, 193 (1979); **94**, 37 (1980).
[22] A. Denner, S. Dittmaier, M. Roth, and M. M. Weber, Nucl. Phys. **B660**, 289 (2003).
[23] K. Hagiwara and D. Zeppenfeld, Nucl. Phys. **B274**, 1 (1986); **B313**, 560 (1989).
[24] S. Dittmaier, Phys. Rev. D **59**, 016007 (1998).
[25] G. Passarino and M. J. Veltman, Nucl. Phys. **B160**, 151 (1979).
[26] W. Beenakker, PhD thesis, Leiden University, 1989.
[27] G. Duplancic and B. Nizic, Eur. Phys. J. C **20**, 357 (2001).
[28] S. Dittmaier, Nucl. Phys. **B675**, 447 (2003).
[29] A. Denner, U. Nierste, and R. Scharf, Nucl. Phys. **B367**, 637 (1991).
[30] W. Beenakker and A. Denner, Nucl. Phys. **B338**, 349 (1990).
[31] T. Hahn and M. Perez-Victoria, Comput. Phys. Commun. **118**, 153 (1999).
[32] A. Denner and S. Dittmaier, Nucl. Phys. **B658**, 175 (2003); Nucl. Phys. **B734**, 62 (2006).
[33] T. Binoth *et al.*, J. High Energy Phys. 10 (2005) 015.
[34] T. Stelzer and W. F. Long, Comput. Phys. Commun. **81**, 357 (1994); F. Maltoni and T. Stelzer, J. High Energy Phys. 02 (2003 027); J. Alwall *et al.*, J. High Energy Phys. 09 (2007) 028.
[35] F. A. Berends *et al.*, Nucl. Phys. **B206**, 61 (1982); R. Kleiss, Z. Phys. C **33**, 433 (1987).
[36] W. T. Giele and E. W. N. Glover, Phys. Rev. D **46**, 1980 (1992).
[37] L. Reina, S. Dawson, and D. Wackeroth, Phys. Rev. D **65**, 053017 (2002).
[38] A. Denner, S. Dittmaier, M. Roth, and D. Wackeroth, Nucl. Phys. **B587**, 67 (2000).
[39] A. Denner, Fortschr. Phys. **41**, 307 (1993).
[40] J. Pumplin, D. R. Stump, J. Huston, H. L. Lai, P. Nadolsky, and W. K. Tung, J. High Energy Phys. 07 (2002) 012.
[41] S. Catani, Yu. L. Dokshitzer, and B. R. Webber, Phys. Lett. B **285**, 291 (1992); S. Catani, Yu. L. Dokshitzer, M. H. Seymour, and B. R. Webber, Nucl. Phys. **B406**, 187 (1993); S. D. Ellis and D. E. Soper, Phys. Rev. D **48**, 3160 (1993); G. C. Blazey *et al.*, in *Proceedings of the Physics at Run II: QCD and Weak Boson Physics Workshop*, edited by U. Baur, R. K. Ellis, and D. Zeppenfeld (Fermilab, Batavia, 2000) (Report No. FERMILAB-PUB-00-297, 2000).
[42] G. Bozzi, B. Jäger, C. Oleari, and D. Zeppenfeld, Phys. Rev. D **75**, 073004 (2007).